ADVANCED MATERIALS

Supporting Information

for *Adv. Mater.,* DOI: 10.1002/adma.202209089

A Polymorphic Memtransistor with Tunable Metallic and Semiconducting Channel

Yonas Assefa Eshete, Eunji Hwang, Junhyung Kim, Phuong Lien Nguyen, Woo Jong Yu, Bai Sun Kong, Min Seok Jang, Jaekwang Lee, Suyeon Cho, and Heejun Yang**

WILEY-VCH

Supporting Information

A Polymorphic Memtransistor with a Tunable Metallic and Semiconducting Channel

Yonas Assefa Eshete, Eunji Hwang, Junhyung Kim, Phuong Lien Nguyen, Woo Jong Yu, Bai Sun Kong, Min Seok Jang, Jaekwang Lee, Suyeon Cho, Heejun Yang**

Dr. Y. A. Eshete,
Department of Energy Science, Sungkyunkwan University, Suwon 16419, Korea

J. Kim, Prof. M. S. Jang
School of Electrical Engineering, Korea Advanced Institute of Science and Technology (KAIST), Daejeon 34141, Korea

P. L. Nguyen, Prof. J. Lee
Department of Physics, Pusan National University, Busan 46241, Korea

Prof. W. J. Yu, Prof. B. S. Kong
Department of Electrical and Computer Engineering, Sungkyunkwan University, Suwon 16419, Korea

Prof. S. Cho
Department of Chemical Engineering and Materials Science, Ewha Womans University, Seoul, 03760, Korea
Email: s.cho@ewha.ac.kr

Prof. H. Yang
Department of Physics, Korea Advanced Institute of Science and Technology (KAIST), Daejeon 34141, Korea
Email: h.yang@kaist.ac.kr

A

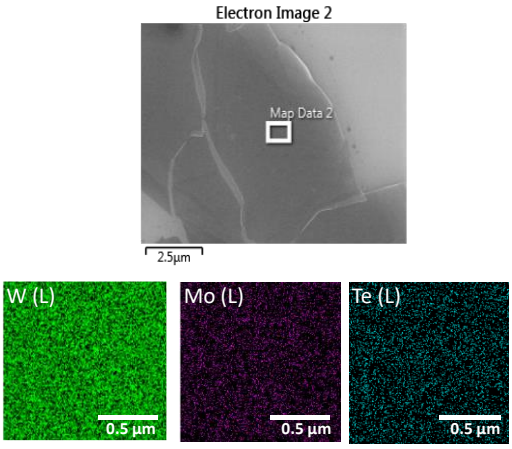

B

x	Mo (At%)	W (At%)	Te (At%)
1T' $MoTe_2$	33.12	0	66.88
0	33.41	0	66.59
0.05	31.79	1.59	66.62
0.07	31.06	2.35	66.59
0.09	30.77	3.05	66.18
0.1	30.39	3.47	66.14
0.3	23.67	9.89	66.44
0.5	16.73	17.02	66.25

Figure S1. The compositional characterization of the $W_xMo_{x-1}Te_2$ alloy. A, SEM-EDS elemental mapping of the Mo (L serious), W (L serious) and Te (L serious) atoms of $W_{0.5}Mo_{0.5}Te_2$ which demonstrate the uniform spatial distribution of each constituent element. **B,** Table for stoichiometric (nominal) composition (x, $W_xMo_{x-1}Te_2$) and corresponding atomic percent amount of each element from SEM-EDS spectrum.

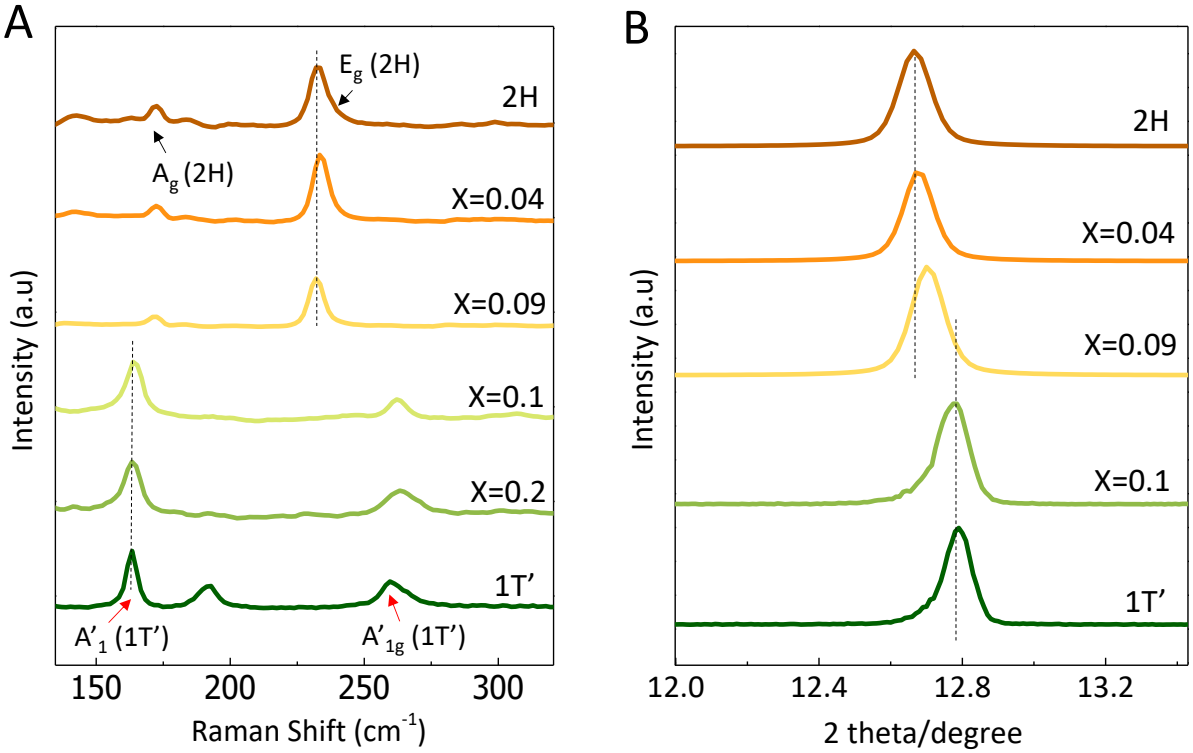

Figure S2. Structural Phase transition in single crystal $W_xMo_{x-1}Te_2$ alloy. A, Tungsten (W) composition dependent Raman spectrum. The red arrows indicate the emergence of the new Raman peak of the 1T' phase while the black arrow indicates the disappearance of Raman peak associated with the 2H phase without any mixed peak coexistence. Demonstrating the sharp structural transition from the 2H to 1T'phase (black arrow). **B,** Composition dependent XRD peak along the (002) crystal plane. demonstrates a consistent 2H(α) to1T'(β) phase transition.

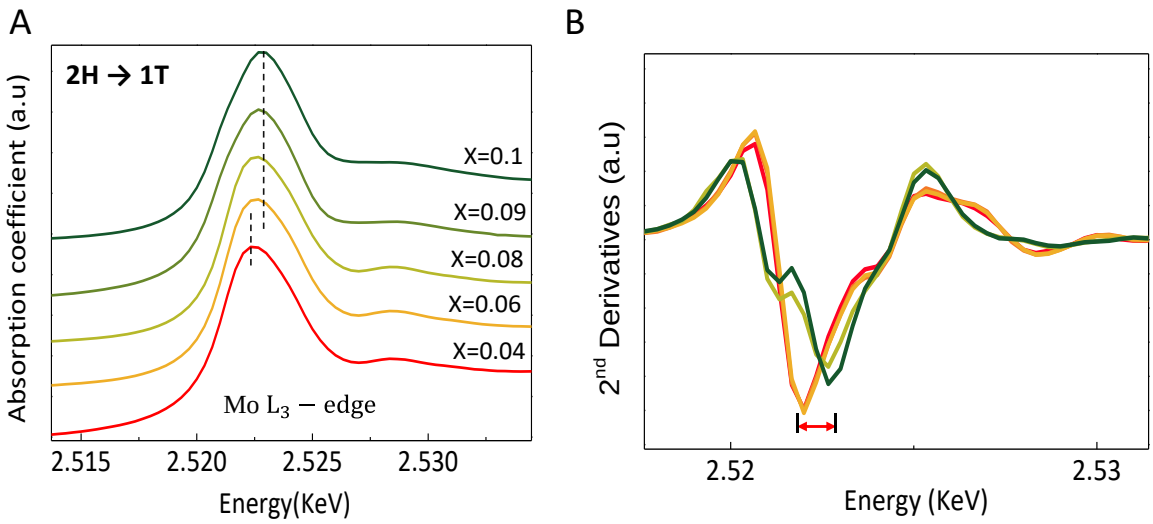

Figure S3. Structural Phase transition in single crystal $W_xMo_{x-1}Te_2$ alloy. A, Tungsten (W) composition dependent Xay absorption spectroscopy (XAS) measurement of the Mo L-edge of the $Mo_{1-x}W_xe_2$ alloy. **B,** Composition dependent second derivative XAS spectrum of Fig. A. The structural phase transition from the semiconducting (2H) phase to the metallic (1T') phase observed at a critical W composition of x = 0.1, demonstrating an XPS peak shift of 0.25 eV. The red double arrow indicates the XPS edge shift between 2H and 1T' phases.

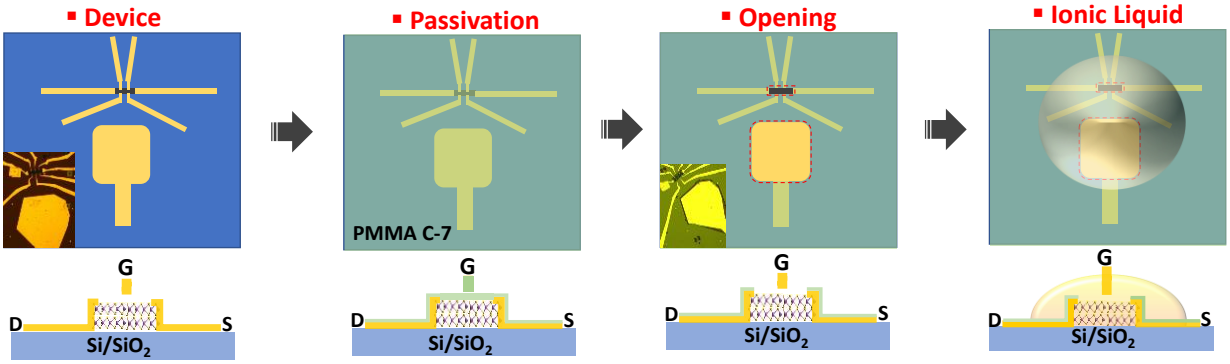

Figure S4. Electric double layer transistor (EDLT) device fabrication with $Mo_{0.91}W_{0.09}Te_2$ alloy. A few layers (2-4 layers) of $Mo_{0.91}W_{0.09}Te_2$ alloy crystal were exfoliated to fabricate a device with a hall-bar structure and an isolated top gate electrode constructed to control the gate bias. Only the device channel and gate pad are exposed to the ion gale while all remaining device parts are passivated with PMMA-C7. The ion gel was added inside an Ar filled glove box, and before the measurement started the device was annealed (100 ^{0}C) at high vacuum (10^{-6} torr) for over 12 hours to remove any moisture absorbed by the ionic liquid.

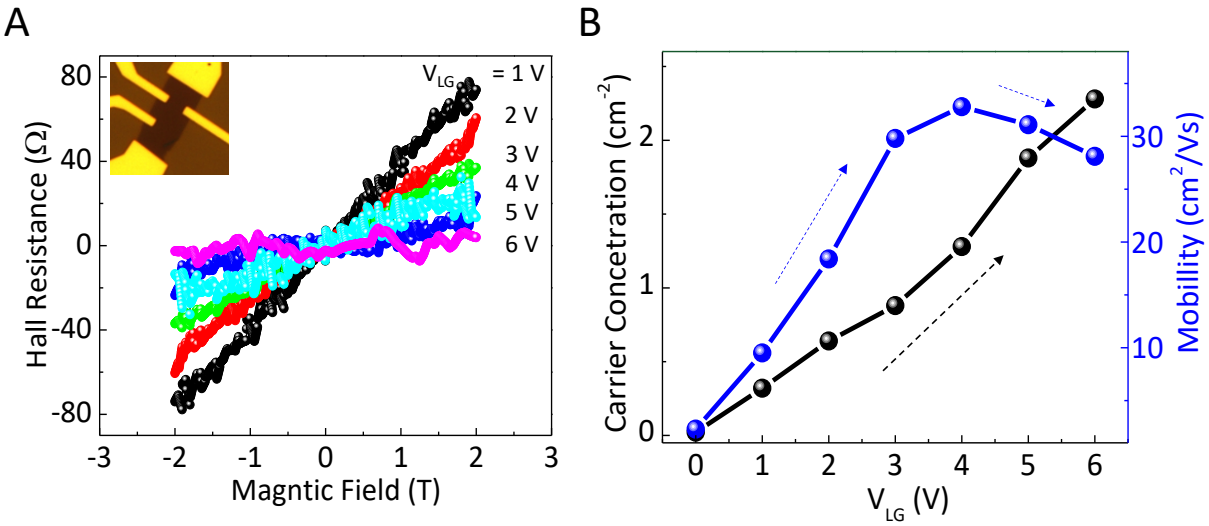

Figure S5. Carrier concentration and capacitance measurement in the $Mo_{0.91}W_{0.09}Te_2$ EDLT device. A, Hall resistance (R_{xy}) of $Mo_{0.91}W_{0.09}Te_2$ at various gate voltages. Inset shows an optical image of the bilayer $Mo_{0.91}W_{0.09}Te_2$ hall bar structure. **B,** Gate dependent carrier concentration (black curve) and corresponding mobility (blue curve) in the $Mo_{0.91}W_{0.09}Te_2$ EDLT device. The carrier accumulation surpasses 10^{14} cm^{-2} just at 3V gate bias, whereas the mobility start decreases above 4V gate bias, which originated from electron-electron scattering due to high carrier accumulation. Capacitance of the ionic liquid can be measured from the slope in panel B, (C_{IL} = d ($n_{2D}e$)/d(Vg), C_{IL} =8.5×10^{-6} F/cm^{-2}.

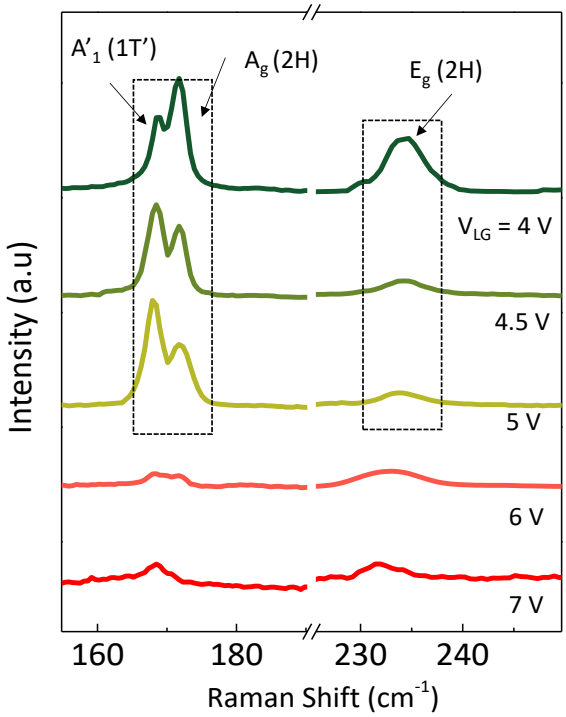

Figure S6. Persistence of 2H phase in gated bilayer $Mo_{0.91}W_{0.09}Te_2$. A, Gate dependent in-situ Raman spectra of the bilayer $Mo_{0.91}W_{0.09}Te_2$ device. The characteristic Raman peaks of the 2H phase A_g (2H) and E_g (2H) remain visible up to 7V gate voltage. At a higher gate voltage, Raman quenching (reduction in overall intensity) was observed, which could be from the Pauli blocking effect.

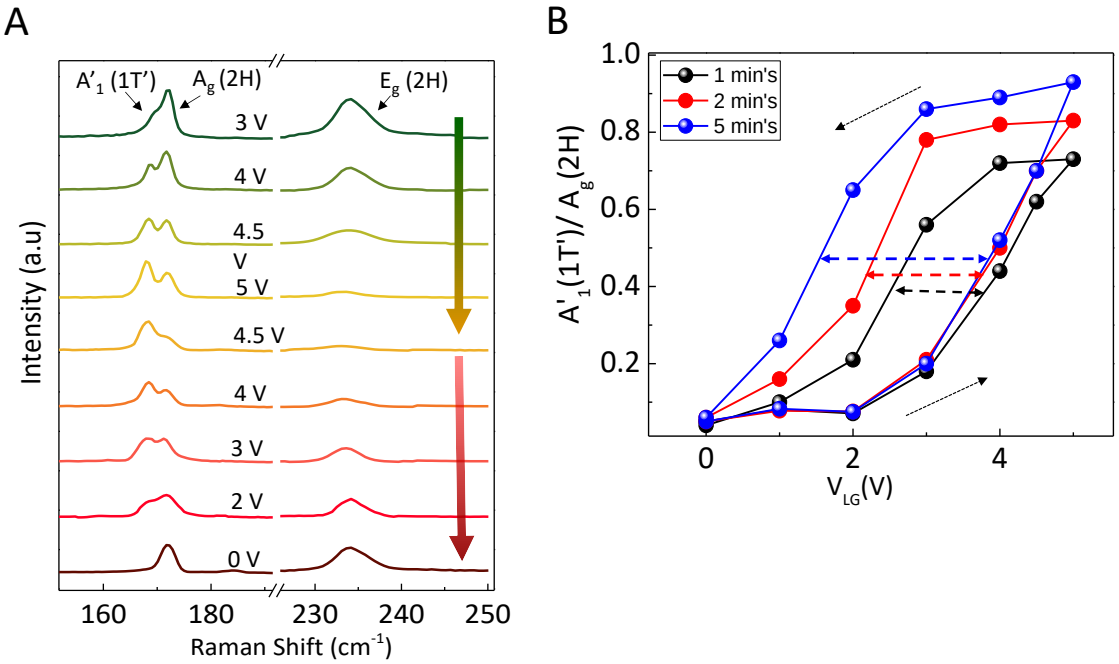

Figure S7. Reversable structural phase transition in $Mo_{0.91}W_{0.09}Te_2$ at various gate scan rates. A, Representative gate dependent in-situ Raman spectra under forward and reverse gate sweeps. Each point Raman was taken after 5 mins waiting time under a specific gate bias. The total time taken to complete the measurement was almost equal to a 5 mV/sec scan rate, which is the slowest scan rate. The greenish and reddish arrow indicates the forward and backward gate scan direction. **B,** Gate-dependent Raman intensity ratios measured as a function of gate voltage scan (forward and backward sweep). The ratio of $A'_1(1T')/A_g(2H)$ shows both increasing tendency which is attributed to the phase transition to the 1T' phase, and the hysteresis which is attributed to the non-volatility of the phase transition. The hysteresis loop or the memory window increases with decreasing scan rate at the gate voltage. The black and red dotted arrows indicate the forward, and the backward sweep, respectively. The double dotted arrows indicate the memory window.

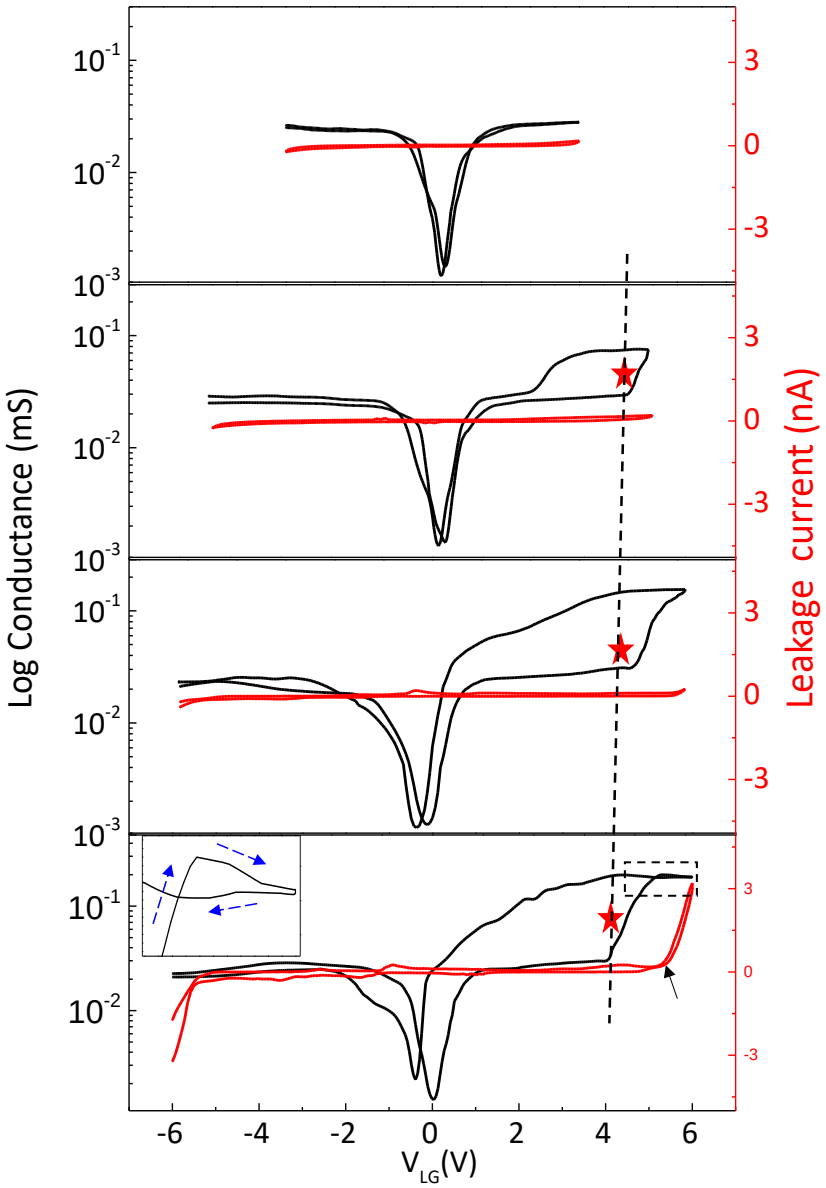

Figure S8. Device performance of $Mo_{0.91}W_{0.09}Te_2$ EDLT at various gate voltage ranges. A, The conductance, and corresponding leakage current evolution of the $Mo_{0.91}W_{0.09}Te_2$ EDLT at 4 different gate voltage sweep ranges, 3V, 4.5V, 5V and 6V, from the topmost panel to the bottom-most panel, respectively. As the gate voltage range increases (from top to bottom panel) we observed a new feature (reduction in resistance or increase in conductance) around a critical gate voltage of 4.1V, which corresponds to a first order structural phase transition from the semiconducting 2H phase to the metallic 1T' phase of $Mo_{0.91}W_{0.09}Te_2$. Below 5V gate sweep range, the leakage current was recorded below the nA current level, whereas above 5V it significantly increased above nA, due to electrochemical effects. The decreasing conductance tendency above V_{LG}=5V is shown in the bottom inset.

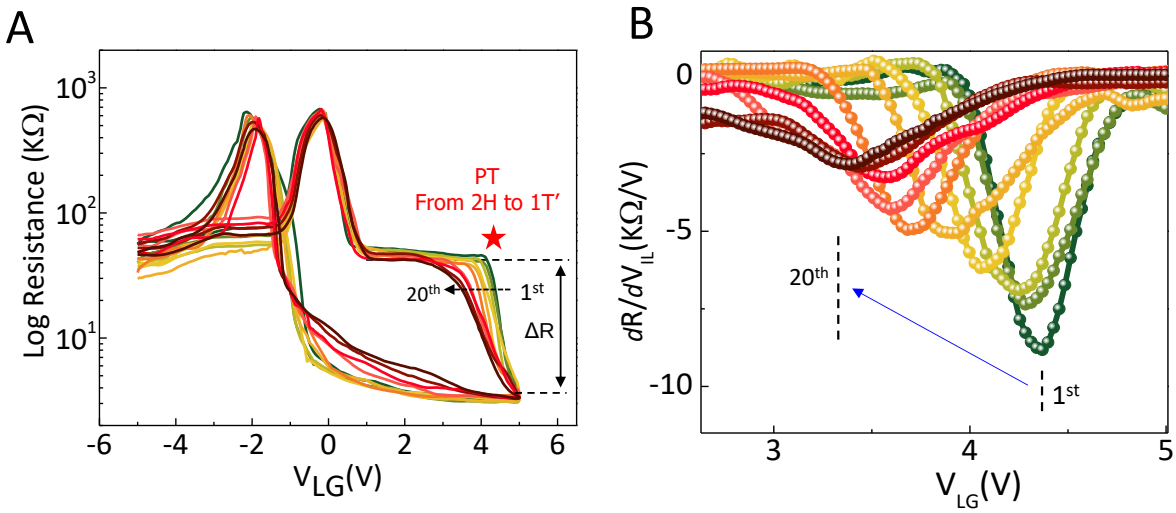

Figure S9. Reliability of the electrostatic gating induced structural phase transition in $Mo_{0.91}W_{0.09}Te_2$. A, The gate dependent resistance measurements over 20 cycles. A reversible phase transition is shown above 20 cycles (20mV/sec, over 7h). **B,** first derivative curve of the gate dependent resistivity over 20 complete cycles (from a forward scan of Fig. A). The blue arrow indicates a decrease in critical phase transition voltage from the 1st to 20th cycle.

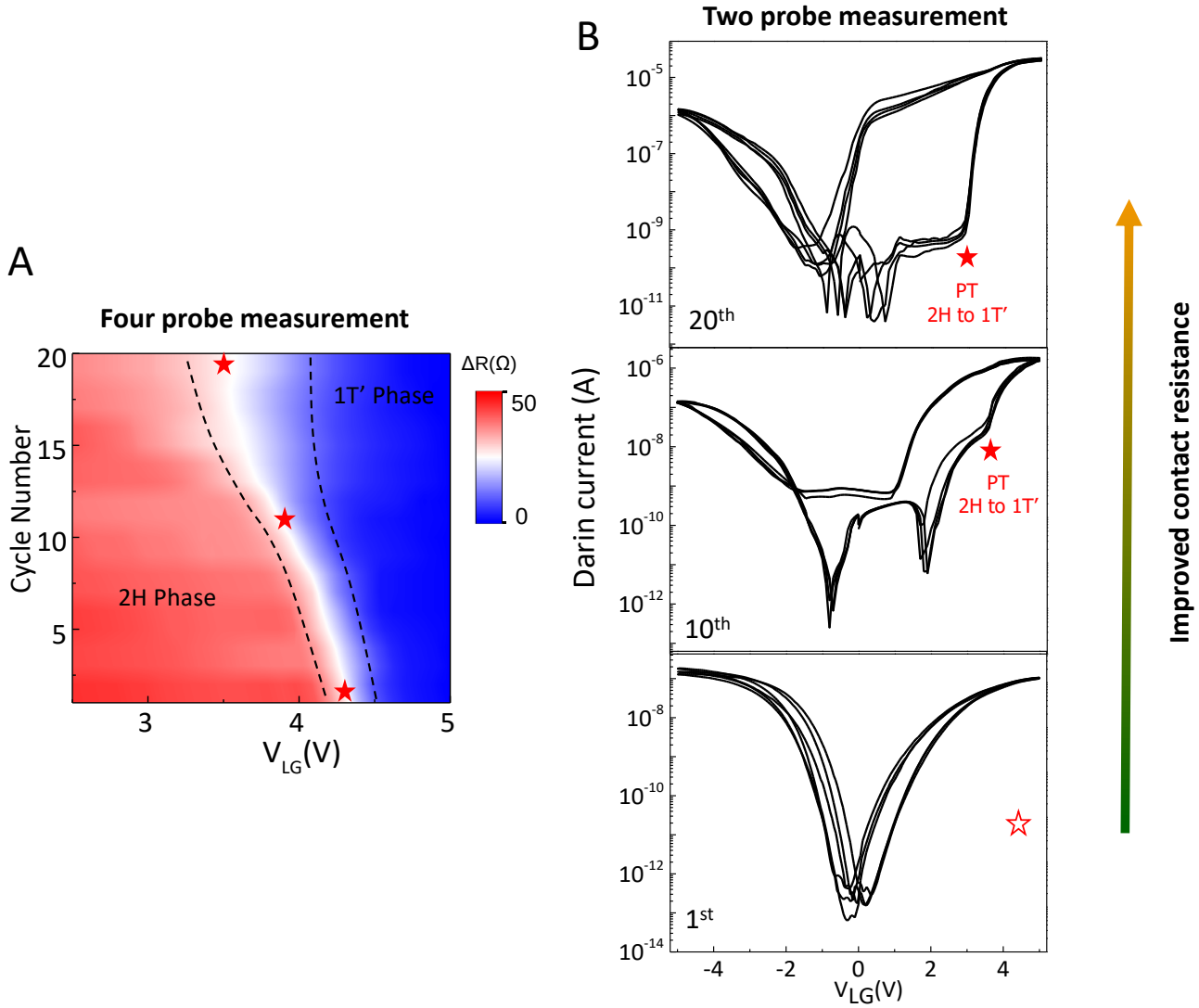

Figure S10. Reliability, device thinning, and contact improvement by ionic gating. A, Contour map of the difference in resistance between the forward and backward sweeps near the gate bias critical for the phase transition (forward scan in Fig. S9, A). The red (high resistance state) and blue (low resistance state) colors indicate the semiconducting (2H) phase and the metallic (1T') phase, respectively. The white region (between the two black-dotted curves) exhibits the onset of the phase transition, which gradually decreases as the cycle number increases. **B,** three transfer curves by V_{LG}. The typical ambipolar transfer curve is observed without any phase transition before the electroforming process (the black curve in the left panel). As the forming process continues, an abrupt increase in current and memory behavior is observed with positive V_{LG}, with electron accumulation.

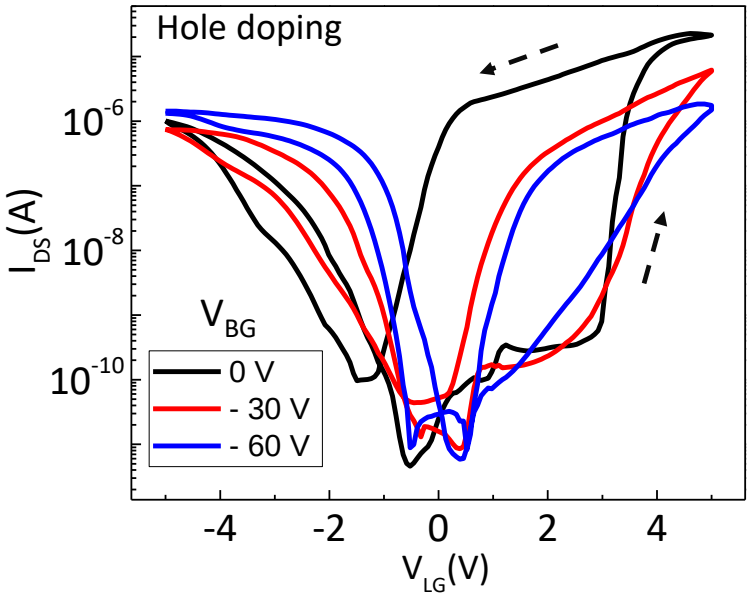

Figure S11. Electrostatic tuning of the phase transition in $Mo_{0.91}W_{0.09}Te_2$. Dual gate transfer curve measurement of electrochemically thinned monolayer sample under negative bottom gate. With hole doping (negative bottom gate) the device loses its characteristic transfer curve of phase transition and displays typical ambipolar device characteristics, which indicates the hole doping has a suppressing effect on the phase transition.

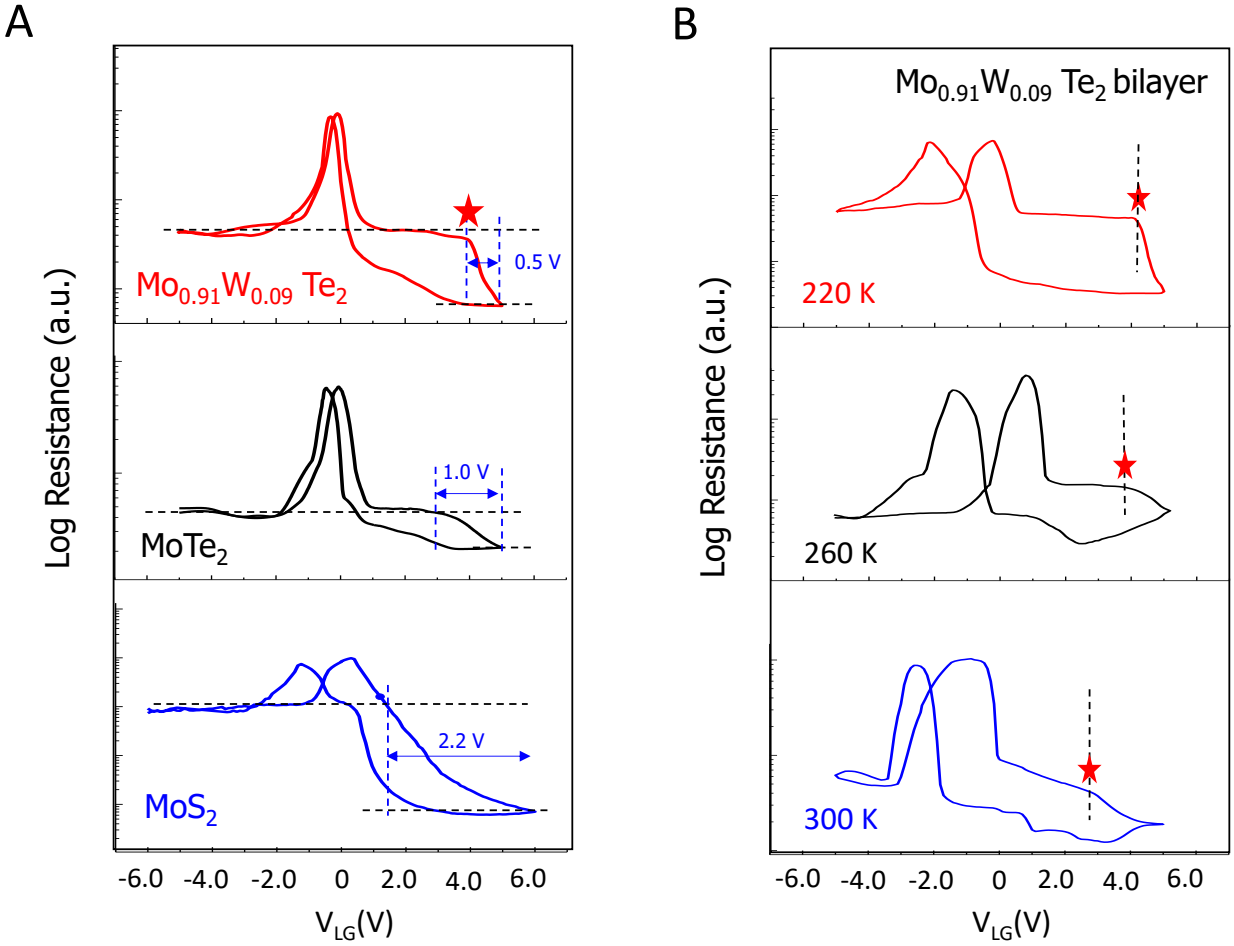

Figure S12. Electrostatic tuning of phase transition in $Mo_{0.91}W_{0.09}Te_2$. A, Gate dependent resistance measurement of various samples of pristine 2H $MoTe_2$, 2H $Mo_{0.91}W_{0.09}Te_2$ and MoS_2. The transport signature of a reversable structural phase transition was clearly observed only in the 2H $Mo_{0.91}W_{0.09}Te_2$ device (top panel) whereas no such feature was observed in the MoS_2 device (bottom panel) for a limited transition in pristine $MoTe_2$. **B**, Transport signature of structural phase transition at various temperatures. The red asterisk the represents critical voltage of the phase transition.

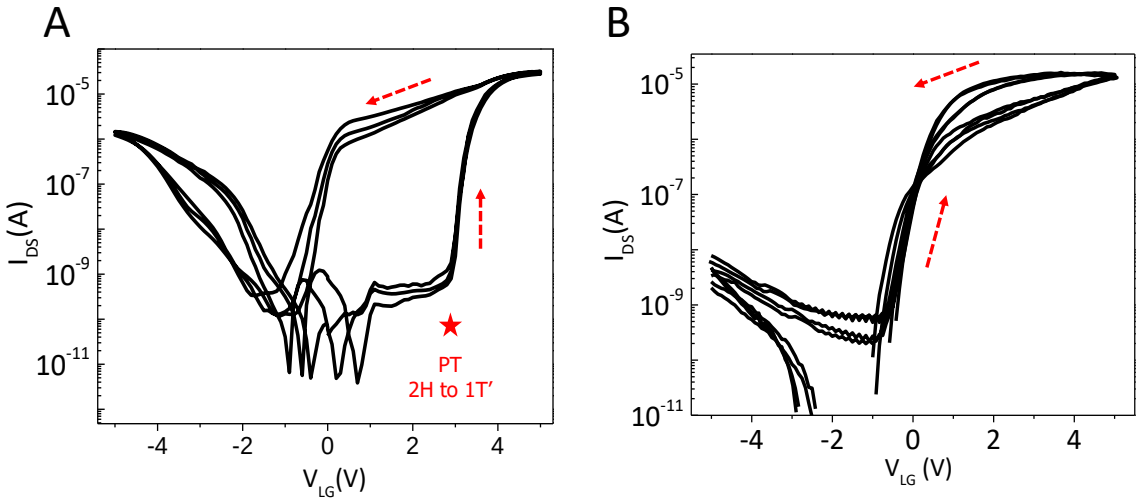

Figure S13. Gate dependent transfer curve in the 2H- $Mo_{0.91}W_{0.09}Te_2$ and MoS_2 EDLT devices. (A-B) Gate dependent two terminal transfer curve of the 2H $Mo_{0.91}W_{0.09}Te_2$ device (panel A) and the 2H MoS_2 device (panel B). It shows a sharp conductance modulation around the gate voltage, 3.5V, as well as the wider memory window associated with the structural phase transition, while the MoS_2 device doesn't show such features.

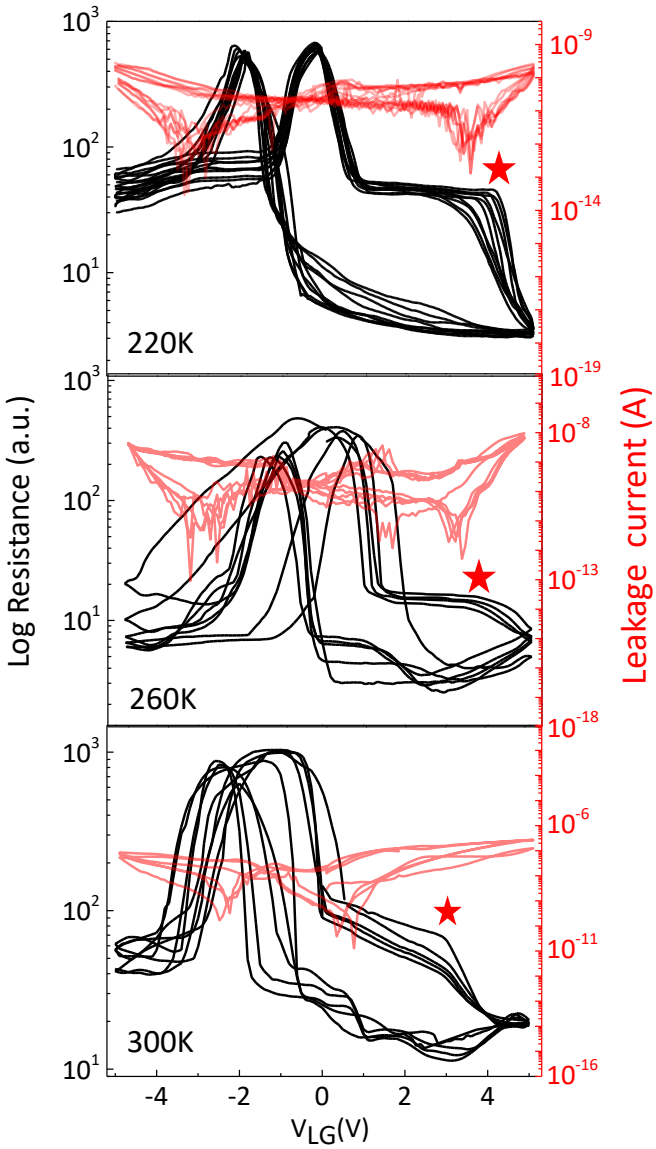

Figure S14. Structural phase transition of $Mo_{0.91}W_{0.09}Te_2$ at various temperatures. The four probe resistance (black curve) and the corresponding leakage current (red curve) of the $Mo_{0.91}W_{0.09}Te_2$ EDLT device. Transport signature of the structural phase transition at various temperatures, indicated by the red asterisk. The critical voltage of phase transition shows a decreasing tendency as the temperature increases. The leakage current surpasses the nA level at temperatures above 260K.

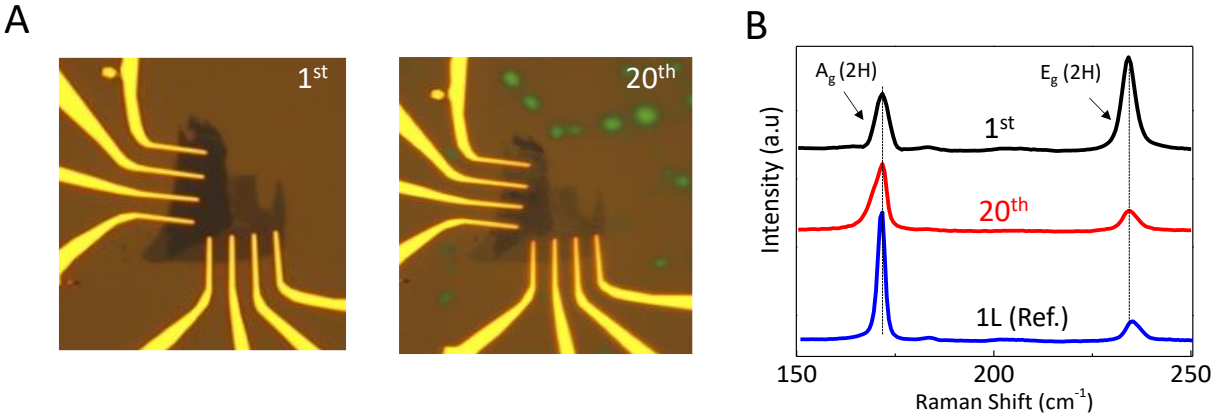

Figure S15. Reliability, device thinning, and contact improvement by ionic gating. A-B, Representative optical image and Raman spectra taken at various cycle number of the devices.